ASSESSING EFFECTS OF SEA-BED AND SEA-SURFACE SCATTERING ON ACOUSTIC PROPAGATION

S Ivansson Swedish Defence Research Agency (FOI), Stockholm, Sweden
T Jenserud Norwegian Defence Research Establishment (FFI), Horten, Norway

1 INTRODUCTION AND SUMMARY

The bistatic impulse response of the underwater acoustic channel is important in connection with underwater communication, for example. Measurements of the shallow-water channel impulse response often indicate long tails, which are not captured by traditional 2-D propagation modelling. It appears that out-of-plane reverberation of forward-scatter type is important to explain these tails.[1-4]

One of the measurement data cases from Ref. 4 is further studied in the present paper. As described in Sec. 2, it is a bistatic 6 kHz shallow-water case with irregular bottom topography. The measured impulse response is modelled with Rev3D, a 3-D ray model described in Sec. 3. Rays are traced from the source to vast numbers of scatterer patches on the water-column interfaces and onwards to the receiver. The contribution from each patch to the impulse response consists of a double sum over transmit and receive rays, with propagation-loss factors coupled by the pertinent 3-D differential cross section scattering kernel. A low-order perturbation theory expression is applied for scattering from the rough sea-bottom, while a composite roughness model is used for the sea-surface scattering.

Section 4 contains the Rev3D results for the data case, with reasonably good match to the measured impulse response. Efforts are made to locate the parts of the water-column interfaces with significant contributions to the impulse response. Energy-density maps for selected time intervals are used for this purpose. Specially constructed time traces for energy-weighted averages of auxiliary parameters, such as the bistatic angle and the ray emission angles, are also used. Features of the bottom topography are noted in the energy-density maps, out-of-plane scattering is seen to be important to explain the impulse-response tails, and major forward-scattering contributions are identified.

The Rev3D reverberation computations with a double sum over transmit and receive rays, for each scatterer patch, are computationally demanding when many rays are traced. For separable scattering kernels, with different factors for the transmit and receive grazing angles, the received energy can be computed much faster as a product of two single sums that are updated as the ray-tracing proceeds. Extending a ray-group technique from Ref. 5, used for accurate time positioning of the scattered energy, Sec. 5 proposes single-sum approximations for the non-separable perturbation theory and composite roughness model kernels. Mainly based on grazing angles and traveltime deviations, groups of rays are formed for which the scattering-kernel values differ in a similar way from certain partially separable approximations. As the ray tracing proceeds, representative grazing angles and interface tangential ray-direction vectors are computed for each patch and ray group, allowing kernel correction factors to be applied when summed quantities for rays in transmit and receive ray groups are multiplied. Reasonably accurate results can be obtained within a fraction of the original CPU time.

2 MEASUREMENT DATA CASE

The data were collected in a Norwegian fjord as part of a channel characterization experiment. A short track, with source-receiver range 0.85 km, is considered here. Source (K2) and receiver (B3) are mounted in stationary frames on sea mounts at water depths around 70-80 m, as shown in the left panel of Fig. 1. Bottom topography is rather complex, with signaling path along a ridge. The bottom consists of a soft sediment layer, with average grain size M_z about 6-8 (phi units) according to grab samples, over hard bedrock. The thickness of the sediment layer is not known, but multibeam measurements indicate relatively high reflectivity and hence thin sediment layer over the ridge along the signaling path. A typical root-mean-square (rms) roughness for the present sediment type is around 1 cm according to Sec. 6.6 in Ref. 6. For the modelling a larger roughness height, 5 cm, is

selected to accommodate two effects: a coarse top surface fraction (the fine fraction is washed out by currents), and roughness scattering from the underlying hard boundary.

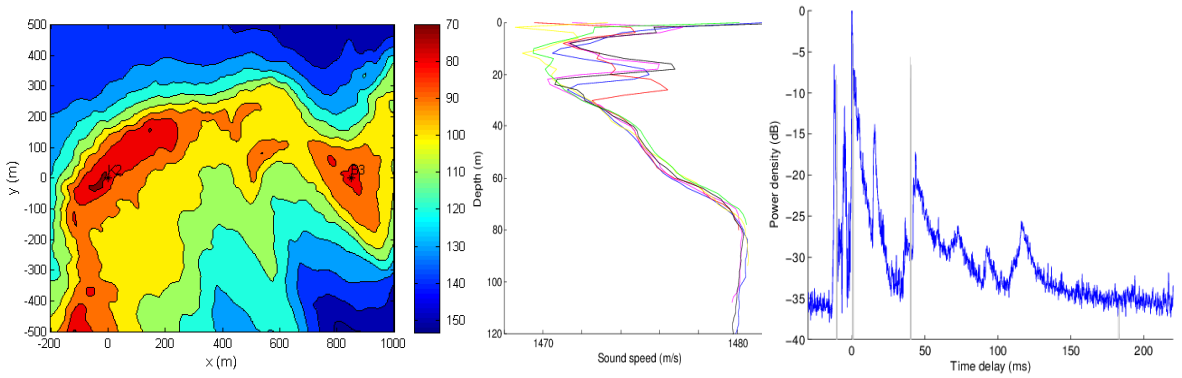

Figure 1. Bottom topography (left), sound speed profiles (middle), and channel impulse response (right). The blue curve is measured channel impulse response, while the grey curve is impulse response computed by a 2-D ray tracer.

Measured sound speed profiles, shown in the middle panel of Fig. 1, display large variability in the upper 30 m, while below 30 m the conditions are much more stable; the sound speed increases down to 80 m depth, and then decreases. Winds were low, 2-5 m/s, during the entire measurement period. The sea state was also low and there was no precipitation.

Channel soundings employed the frequency band from 4 to 8 kHz. The probe signal is a 256 ms Linear Frequency Modulation (LFM) signal which is repeated 64 times over a total of 16.4 s during one transmit cycle. Measured channel impulse responses, Fig. 1 right panel, show complex arrival structures, with arrivals coming in at large separations, each followed by a decaying tail. The total length of the impulse response is not captured by the probe signal, hence the signal does not reach the noise floor before the onset of a new probe. A 2-D ray tracer does not capture the dense arrival structure of the measured impulse response, as seen in the right panel of Fig. 1.

3 THE RAY MODEL REV3D

Rev3D is a 3-D ray model for computation of propagation-loss curves as well as time series for reverberation and propagation.[5,7] Rays from the source are traced with different azimuths as well as elevations. The sound speed c in the water is represented by range-independent profiles within horizontal rectangles. For each rectangle profile, c has a "$1/c^2$ piece-wise linear" variation with depth. Hence, each ray is built up as a sequence of parabolic arcs. Bottom depths are given at the grid points for the horizontal rectangles, and bilinear interpolation is used in between. The intersections of a ray with the bottom can be calculated quickly by solving second-degree polynomial equations.

All energy flow is confined to the thin rays. Average intensities at the receiver are computed for box volumes, obtained by a polar grid centred at the source in the horizontal plane and a division of the depth axis. Each ray contributes to the average for a particular box according to the energy it carries and its arc-length within that box. Propagation loss curves can be produced in selected bearing directions from the source. The propagated energy is positioned on a time axis, and time traces for pressure magnitude space averages in the different receiver boxes are readily obtained.

Bottom and surface reverberation are treated separately, based on computation of average intensities at interface patches. These patches or area elements are formed from a polar grid centred at the receiver, and rays are traced from the receiver as well as the source. For separable scattering kernels, source-to-patch and patch-to-receiver terms can be summed separately for each patch, speeding up the computations significantly. In the present paper, contributions from different rays are added incoherently (power sums), but options for coherent computations have also been developed.[8]

3.1 Intensity Time Traces for Reverberation

Bottom and surface reverberation are handled analogously. In each case, the reverberation time trace for intensity is built up by contributions from each interface patch. Focusing on a particular patch with area dA, its contribution $\varphi(t)$ at time t for a Dirac intensity pulse $\delta(t)$ from the source can be written

$$\varphi(t) = \sum_u \sum_v T_u \, R_v \, S_{u,v} \, \delta(t - t_{\mathrm{T},u} - t_{\mathrm{R},v}) \; . \qquad (1)$$

The sums on u and v are for the transmit (from source to patch) and receive (from patch to receiver, but by reciprocity computed from receiver to patch) ray paths, respectively. The corresponding traveltimes are denoted $t_{\mathrm{T},u}$ and $t_{\mathrm{R},v}$. T_u is the average intensity over the patch contributed by ray u multiplied by $(\mathrm{d}A)^{½}$. R_v is defined analogously, while $S_{u,v}$ is the scattering strength (per unit boundary area, 1 m^2, and scattering angle), for the ray angles involved. Apparently, the product $T_u \, R_v$ in Eq. (1) takes care of the propagation loss in the appropriate way.

Reverberation time traces are obtained by incoherent summation of intensity contributions from each patch. For a source intensity pulse $s(t)$, the convolution $\varphi * s(t)$ is formed. The patches should be small enough to map out possible shadow zones, and to provide closely spaced patch points of transmit and receive rays for an accurate time positioning of the reverberation energy. The number of rays should be large enough to give an adequate coverage of the patches with rays of different types.

For separable scattering kernels, such as the Lambert and Chapman-Harris rules, e.g., Ref. 9, $S_{u,v}$ in Eq. (1) can be factorized as $S_{u,v} = s_{\mathrm{T},u} \, s_{\mathrm{R},v}$, with transmit and receive factors $s_{\mathrm{T},u}$ and $s_{\mathrm{R},v}$, respectively. Harrison[10,11] discusses scattering-strength functions $S(\theta_1,\theta_2,\beta)$ that can be written as products with three factors, each depending on only one angle. Here, θ_1 and θ_2 are grazing angles for incoming and outgoing rays, respectively, and β is the bistatic angle (the angle as viewed from the patch between the ray projections on the patch plane). An option with the partially separable approximation $\tilde{S}$ of a general non-separable kernel S according to

$$\tilde{S}(\theta_1, \theta_2, \beta) = [S(\theta_1, \theta_1, \beta) \, S(\theta_2, \theta_2, \beta)]^{1/2} \qquad (2)$$

has been implemented in Rev3D for fast approximate computations, see Sec. 5. Using the ray indices u and v, $\tilde{S}_{u,v} = s_{\mathrm{T},u} \, s_{\mathrm{R},v}$ with $\tilde{S}_{u,v} = \tilde{S}(\theta_1, \theta_2, \beta)$, $s_{\mathrm{T},u} = \left[\tilde{S}(\theta_1, \theta_1, \beta)\right]^{1/2}$, and $s_{\mathrm{R},v} = \left[\tilde{S}(\theta_2, \theta_2, \beta)\right]^{1/2}$.

3.2 Reflection Coefficients

Rays are reflected specularly at the sea bottom and at the sea surface, and the reflection coefficients are functions of grazing angle and frequency. The bottom reflection coefficients additionally depend on the bottom type, while the surface reflection coefficients additionally depend on the wind speed. For each horizontal grid rectangle, the bottom type can be specified as a porosity value or as a layered bottom with geoacoustic parameters for the different layers. The latter option is used in the modelling examples in the present paper, with bottom parameters corresponding to a mean grain size M_z of 6 (phi units), see Table 4.18 in Ref. 9. At 6 kHz, the pertinent bottom loss is small for grazing angles below some 13°, but it increases to about 12 or 13 dB above 30°.

At the sea surface, losses are induced by an absorbing layer of bubbles (Sec. 8.1.1.2.2 in Ref. 9). At 6 kHz and a low wind speed of 3.5 m/s these losses are small, however, and the surface reflection coefficient is close to unity for all grazing angles.

3.3 Scattering Kernels

Physically based scattering kernels have been proposed, that involve statistical roughness information. The small-slope approximation is shown in Ref. 6 to be a good choice for the bistatic cross section of a rough surface. For sea-surface scattering, it is discussed in Ref. 1 and applied in Ref. 3 to model impulse responses with several distinguishable surface-bottom bounce arrivals. In

the present paper, however, a version of the composite roughness model for surface scattering is considered, that is more easily implemented. With θ_1, θ_2, and β as above, it can be expressed as

$$S(\theta_1, \theta_2, \beta) = S_{\mathrm{b}}(\theta_1, \theta_2) + S_{\mathrm{rf}}(\theta_1, \theta_2, \beta) \,, \tag{3}$$

where $S_b(\theta_1,\theta_2)$ is a contribution from bubbles, that does not depend on β, and $S_{rf}(\theta_1,\theta_2,\beta)$ is obtained by interpolation of small roughness scattering S_r and facet scattering S_f.[4] The bubble contribution S_b, important at low grazing angles, is adapted from Eq. (13) in Ref. 1. Close to the specular direction, S_{rf} agrees with the facet term in Ref. 12, see Eq. (2) and Sec. III there. Far from the specular direction,

$$S_{\mathrm{rf}}(\theta_1, \theta_2, \beta) = S_{\mathrm{r}}(\theta_1, \theta_2, \beta) = 4\, k^4 \sin^2(\theta_1) \sin^2(\theta_2)\, G_1(\theta_1, \theta_2, \beta) \,, \tag{4}$$

where k is the wavenumber in the water while G_1 is the isotropic one-dimensional roughness spectrum derived from the Pierson-Moskowitz gravity-wave frequency spectrum for a fully developed sea (Sec. 8.1.2 in Ref. 9). Figure 2 shows some examples relevant to the modelling in Sec. 4.

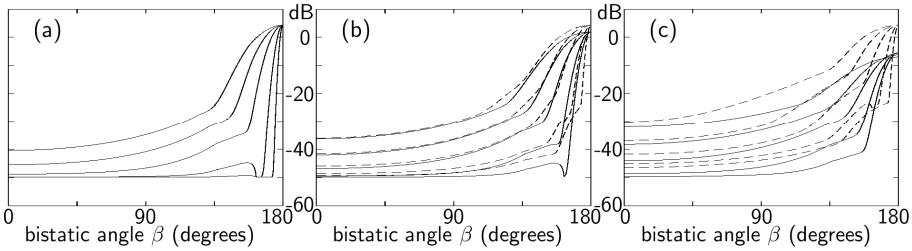

Figure 2. Composite roughness sea-surface scattering strength S as function of bistatic angle β at 6 kHz for the wind speed 3.5 m/s. The three panels concern different values of the difference between the grazing angles of the incoming and outgoing rays: (a) 0º, (b) 15º, and (c) 30º. In each panel, the five solid and the five dashed curves show S results and approximate $\tilde{S}$ results (Eq. (2)), respectively, for different values of the least grazing angle: from bottom to top 5º, 10º, 20º, 30º, and 40º.

For the bottom, a low-order small perturbation method (SPM) scattering kernel S is selected, used at the Office of Naval Research (ONR) reverberation modelling workshop 2006. It is specified in Refs. 13 and 14, and it agrees with Eq. (13.9) in Ref. 6, together with Eqs. (13.21), (13.26), and (8.49) there. The bottom-scattering kernel S includes the bottom roughness spectral density W, taken as

$$W(\boldsymbol{k}) = (2\pi)^{-1}\, h^2\, k_l\, (k_l^2 + |\boldsymbol{k}|^2)^{-3/2} \tag{5}$$

where $\boldsymbol{k}$ is the wavenumber vector, h is the rms roughness height, and k_l is the inverse of the correlation length l of the roughness. This SPM kernel is most accurate for scattering at wide angles relative to the specular direction. Close to the specular direction, the Kirchhoff or small-slope approximations would be better. Figure 3 shows some relevant examples.

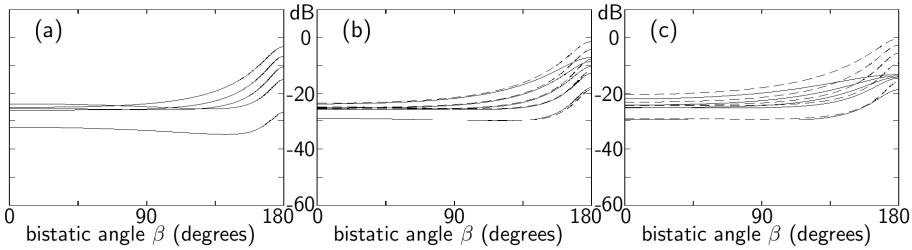

Figure 3. SPM sea-bottom scattering strength S as function of bistatic angle β at 6 kHz. The bottom sound speed and density correspond to a mean grain size M_z of 6 (phi units)*. The roughness height h and correlation length l are taken as 5 and 25 cm, respectively. In the same way as in Fig. 2, there are three panels with five solid and five dashed curves in each panel.*

The selected scattering kernels are symmetric in θ_1 and θ_2, since all quantities involved are.

4 MODELLING RESULTS

The left panel of Fig. 4 shows Rev3D results for a bottom with sound speed and density corresponding to a mean grain size Mz of 6 (phi units). The bottom roughness height *h* and correlation length *l* are 5 and 25 cm, respectively, and the wind speed is 3.5 m/s. Some ten million rays are traced from the source as well as from the receiver. The interface patches in the polar grid centred at the receiver have a width of two degrees azimuthally and a length of four m radially (except close to the receiver where they are smaller). The source pulse is centred at 6 kHz with length 0.25 ms after match-filtering.

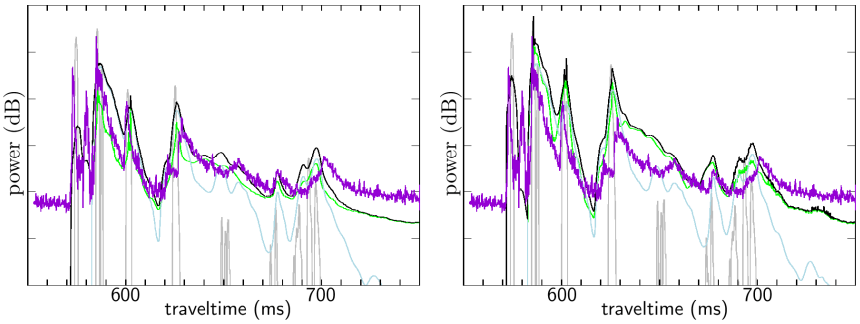

Figure 4. Modelled and measured time series, with 10 dB between tick marks on the vertical axis. In each panel, the black, green, and blue curves concern modelled total, bottom, and surface reverberation, respectively. There is also a spiky grey curve, which only includes modelled propagation. The violet curve shows the measured data. The right panel is included for comparison, with modelling according to the Ellis-Crowe semi-empirical bottom scattering kernel[12,9] as in Ref. 4.

The peaks followed by tails in the measured data are reasonably well matched by the modelled traces. Some reverberation peaks (in violet and black) agree with modelled propagation peaks (in grey).

For the right panel of Fig. 4, with reasonably similar results, the bottom scattering is modelled with a semi-empirical kernel[12,9] as in Ref. 4, for a bottom with porosity 0.47 and roughness slope angle 9°.

4.1 Spatial scattering origin of reverberation energy

Figure 4 has shown how the reverberation energy is distributed in time. Its distribution in terms of auxiliary parameters, for example grazing and bistatic angles, can also be studied. Figures 5 and 6 show distributions in terms of scattering origin in the horizontal plane of the modelled sea-surface and sea-bottom reverberation energy, respectively. The total surface reverberation energy density is very large in the vicinity of the line segment connecting source and receiver, cf. Refs. 10 and 11, and the energy with traveltime around 700 ms originates mainly from three spots close to this line segment.

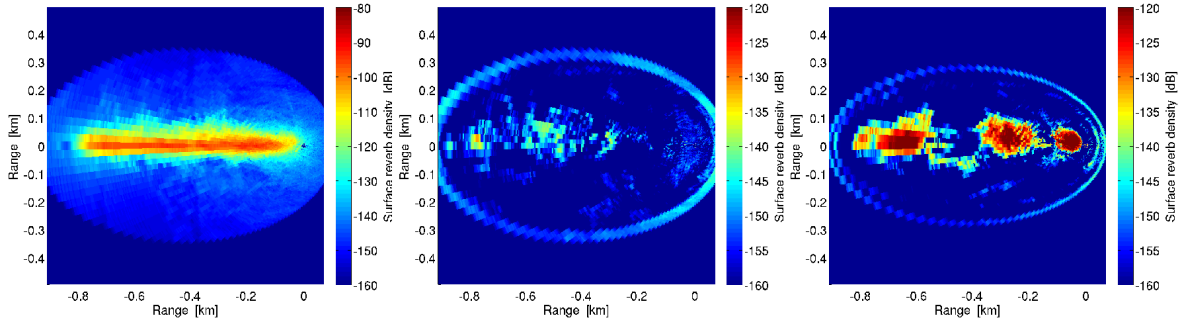

Figure 5. Scattering origin in the horizontal plane of modelled sea-surface reverberation, per unit horizontal surface area (1 m^2) and in dB. The receiver is at the origin in the horizontal coordinate system, with the source 850 m to the left. Energy with traveltime less than 750 ms (left panel), between 720 and 750 ms (middle panel), and between 693 and 701 ms (right panel). Note different dB scales!

The bottom reverberation in Fig. 6 exhibits a concentration near the source-receiver line segment in the left panel, at a surrounding elliptical border in the middle panel, and at two spots close to the source-receiver line segment in the right panel. Compared to the left panel of Fig. 5, the contributions are more spread out, probably because of the source and receiver locations close to the bottom and the upward refracting sound speed profile. The bathymetry with varying depths and slopes, see the left panel of Fig. 1, gives rise to some patterns in the map view. A bottom topography providing higher grazing angles or more roughness at the elliptical border in the middle panel would apparently imply stronger modelled reverberation at late traveltime and a better match to the measured data in Fig. 4.

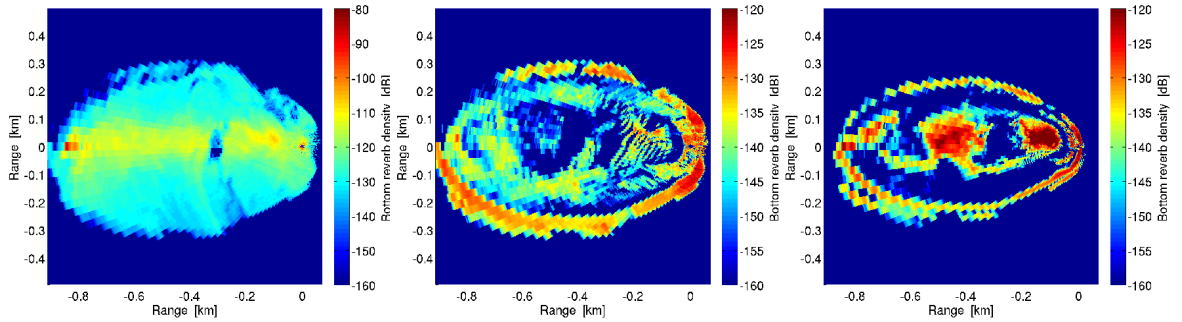

Figure 6. As Fig. 5 but for sea-bottom reverberation.

The high-energy spots in the right panels of Figs. 5 and 6 can be explained by enhanced scattering at the three surface-bounce spots and the two bottom-bounce spots of a few close eigenrays connecting source and receiver. The maps indicate effects of horizontal refraction at the bottom bounces, with the high-energy bounce spots slightly displaced from the source-receiver line segment.

4.2 Time evolution of dominant grazing angles, bistatic angles, etc.

An auxiliary parameter Q, the bistatic angle β, for example, can be studied by the time evolution of its energy-weighted averages. With $Q_{u,v}$ as the auxiliary parameter for ray pair u,v, $q_m(t)$ is defined as

$$q_m(t) = \sum_u \sum_v \, (Q_{u,v})^m \, T_u \, R_v \, S_{u,v} \, \delta(t - t_{\mathrm{T},u} - t_{\mathrm{R},v}) \qquad (6)$$

with notation as in Eq. (1). The time trace $Q_a(t) = q_1 * s(t)/\varphi * s(t)$ for energy-weighted averages of Q can now be formed along with its corresponding standard deviations $Q_s(t) = [\, q_2 * s(t)/\varphi * s(t) - Q_a^2(t) \,]^{1/2}$.

Figure 7 shows time evolution plots of the grazing-angle averages and differences, and the bistatic angle. Panel (c) indicates a clear dominance of forward-scattering contributions, $\cos(\beta)$ close to −1, for traveltimes between 620 and 700 ms. At 572, 585, 602, 625, 678, and 697 ms, deep dips of $\cos(\beta)$ appear where $\theta_1 \approx \theta_2$, see panel (b), implying scattering concentration close to the specular direction. Indeed, Fig. 4 exhibits reverberation as well as propagation peaks at these traveltimes.

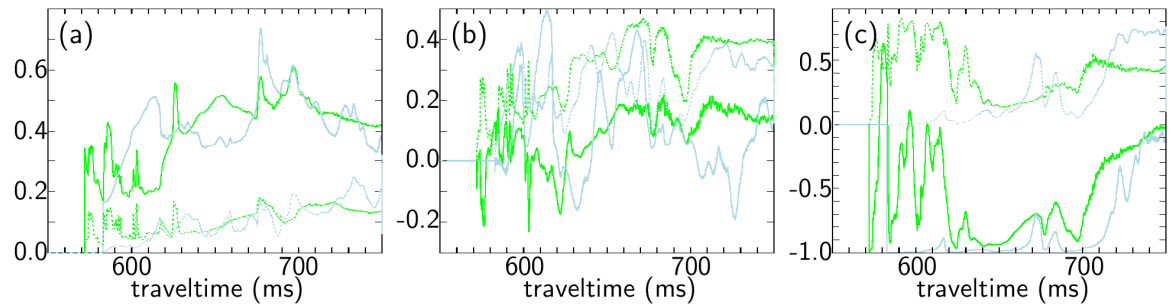

Figure 7. Time evolution of (a) $[\sin(\theta_1)+\sin(\theta_2)]/2$, (b) $\sin(\theta_2)-\sin(\theta_1)$, and (c) $\cos(\beta)$. The green and blue curves concern bottom and surface reverberation, respectively. The solid curves indicate averages, while the dashed ones indicate standard deviations.

5 APPROXIMATING THE SCATTERING KERNELS

A drawback with Eq. (1) is that data for all rays reaching the patch must be stored in order for the double summation to be performed at the end. Moreover, the double summation for each patch for a large number of bottom as well as surface patches requires significant computer time. Approximations are thus of great interest. Theoretically, a general scattering kernel $S_{u,v}$ can be well approximated by a sum $\tilde{S}_{u,v}$ of separable terms, indexed by l according to $\tilde{S}_{u,v} = \sum_{l=1}^{L} s_{\mathrm{T}l,u}\, s_{\mathrm{R}l,v}$. This follows from the Stone-Weierstrass theorem, e.g., Ref. 15. With $S_{u,v}$ replaced by $\tilde{S}_{u,v}$, Eq. (1) takes the form

$$\varphi(t) = \sum_{l=1}^{L} \left(\sum_u \sum_v \, (T_u \, s_{\mathrm{T}l,u}) \, (R_v \, s_{\mathrm{R}l,v}) \, \delta(t - t_{\mathrm{T},u} - t_{\mathrm{R},v}) \right) . \qquad (7)$$

Each l-term in Eq. (7) may now be approximated by a box function.[5] The centre time, width, and height of the box are determined by a few quantities that are updated successively as the ray tracing proceeds, separately for transmit and receive rays. Storing of data for each ray is thus not needed, and the double summation on u and v is replaced by single summations, see Eqs. (4)-(6) in Ref. 5.

As also discussed in Ref. 5, improved box approximations can be obtained by splitting the rays for each patch into groups, according to traveltime or number of interface reflections, for example. Specifically, the transmit and receive rays for a particular patch are divided into m_{T} groups $I_1, I_2, .., I_{m\mathrm{T}}$ and m_{R} groups $J_1, J_2, .., J_{m\mathrm{R}}$, respectively, and $\varphi(t) = \sum_{i=1}^{m\mathrm{T}} \sum_{j=1}^{m\mathrm{R}} \varphi_{i,j}(t)$ where $\varphi_{i,j}(t)$ is defined by

$$\varphi_{i,j}(t) = \sum_{l=1}^{L} \left(\sum_{u:u\in Ii} \sum_{v:v\in Jj} \, (T_u \, s_{\mathrm{T}l,u}) \, (R_v \, s_{\mathrm{R}l,v}) \, \delta(t - t_{\mathrm{T},u} - t_{\mathrm{R},v}) \right) . \qquad (8)$$

Each l-component of each $\varphi_{i,j}(t)$ can now be approximated by a box function, resulting in an improved approximation of $\varphi(t)$. Taylor expansions with L = 48 terms are used in Ref. 14 for a certain scattering kernel in the monostatic case, but alternative function expansions exist (e.g., Ref. 16).

Here, however, a different route is taken. The basic idea is to choose ray groups such that the grazing angles θ are similar within each ray group and the bistatic angles β are similar for the transmit and receive rays of each ray-group pair. With the partially separable approximation $\tilde{S}_{u,v} = s_{\mathrm{T},u}\, s_{\mathrm{R},v}$ from Eq. (2), source-to-patch and receiver-to-patch terms are summed separately for each patch, using an approximate bistatic angle $\tilde{\beta}$ for the patch obtained from straight line segments from the patch centre to the source and to the receiver. For the box-function approximations, Eq. (8) is replaced by

$$\varphi_{i,j}(t) \; = \; \frac{S_{ij}}{s_{\mathrm{T},i}\, s_{\mathrm{R},j}} \sum_{u:u\in Ii} \sum_{v:v\in Jj} \, (T_u \, s_{\mathrm{T},u}) \, (R_v \, s_{\mathrm{R},v}) \, \delta(t - t_{\mathrm{T},u} - t_{\mathrm{R},v}) \;\; , \qquad (9)$$

where S_{ij} is the scattering kernel S computed for representative grazing angles and interface tangential ray-direction vectors of the rays in the ray groups I_i and J_j, respectively. Such representative angles and vectors are computed as the ray tracing proceeds, for each patch and ray group, as energy-weighted averages for incoming and outgoing rays, respectively. The quantities $s_{\mathrm{T},i}$ and $s_{\mathrm{R},j}$ are obtained as the factors $s_{\mathrm{T},u}$ and $s_{\mathrm{R},v}$ computed for the approximate bistatic angle $\tilde{\beta}$ of the patch and the representative grazing angles of the rays in the ray groups I_i and J_j, respectively.

Figure 8 shows an example where ray groups for Eq. (9) are formed with $m_{\mathrm{T}} = m_{\mathrm{R}} = 60$, defined by a combination of grazing angle and traveltime, the latter also to allow accurate time positioning of the reverberation energy. Specifically, twelve grazing-angle bins separated at 5,10,..,85 degrees are combined with five traveltime-excess bins separated at 10,20,30,40 ms, where the traveltime excess is defined relative to a nominal (fast) sound speed in the water. The left panel of Fig. 8 shows a satisfactory agreement to Fig. 4 (left panel). The additional quotient factor in Eq. (9) introduces a scattering-strength correction that is appropriate for the rays in the pertinent ray-group pair. Without it, right panel of Fig. 8, the agreement to Fig. 4 is poor particularly around 610-620 ms. Indeed, Figs. 2 and 3 indicate that S is sensitive to β for large β and that the approximations $\tilde{S}$ from Eq. (2) may be poor for forward scattering (large β) unless the difference between the grazing angles is small.

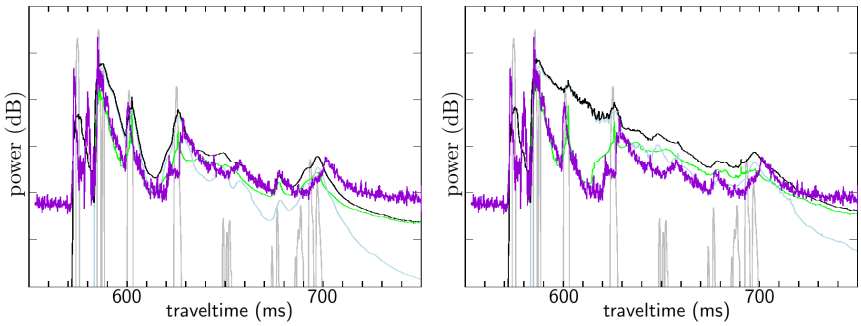

Figure 8. Modelled and measured time series shown in the same way as in Fig. 4, but with modelling based on single summations for box approximations of Eq. (9) involving approximate scattering kernels and ray groups. For the right panel, the quotient correction factor in Eq. (9) is omitted.

The CPU times for complete (Fig. 4) and approximate (Fig. 8) computations were about seven hours and 55 minutes, respectively. For computations involving more rays, or auxiliary parameters with additional storage requirements, the relative time gains will of course increase, when double summations as in Eqs. (1) or (6) are replaced with single summations for box approximations based on Eq. (9).

6 REFERENCES

1. P.H. Dahl, 'On bistatic sea surface scattering: Field measurements and modeling', J.Acoust.Soc.Am. 105(4) 2155-2169. (April 1999)
2. P.H. Dahl, 'High-frequency forward scattering from the sea surface: The characteristic scales of time and angle spreading', IEEE J.Ocean.Eng. 26(1) 141-151. (January 2001)
3. J.W. Choi and P.H. Dahl, 'Measurement and simulation of the channel intensity impulse response for a site in the East China Sea', J.Acoust.Soc.Am. 119(5) 2677-2685. (May 2006)
4. T. Jenserud and S. Ivansson, 'Measurements and modelling of effects of out-of-plane reverberation on the power delay profile for underwater acoustic channels', manuscript submitted to IEEE J.Ocean.Eng. (2015)
5. S. Ivansson, Stochastic ray-trace computations of transmission loss and reverberation in 3-D range-dependent environments, Proc. 8th ECUA, 131-136. Carvoeiro (2006).
6. D.R. Jackson and M.D. Richardson. High-Frequency Seafloor acoustics, Springer. (2007)
7. F. Sturm, S. Ivansson, Y.-M. Jiang and N.R. Chapman, 'Numerical investigation of out-of-plane sound propagation in a shallow water experiment', J.Acoust.Soc.Am. 124(6) EL341-346. (Dec 2008)
8. S. Ivansson, Ray modelling of active sonar element-level time series in 3-D range-dependent environments, Proc. 1st UA. Corfu (2013).
9. M.A. Ainslie. Principles of Sonar Performance Modeling, Springer. (2010)
10. C.H. Harrison, 'Fast bistatic signal-to-reverberation-ratio calculation', J.Comput.Acoust. 13(2) 317-340. (2005)
11. C.H. Harrison, 'Closed form bistatic reverberation and target echoes with variable bathymetry and sound speed', IEEE J.Ocean.Eng. 30(4) 660-675. (2005)
12. D.D. Ellis and D.V. Crowe, 'Bistatic reverberation calculations using a three-dimensional scattering function', J.Acoust.Soc.Am. 89(5) 2207-2214. (May 1991)
13. J.E. Moe and D.R. Jackson, 'Near-field scattering through and from a two-dimensional fluid-fluid rough interface', J.Acoust.Soc.Am. 103(1) 275-287. (January 1998)
14. S. Ivansson, L. Abrahamsson, I. Karasalo and M. Ainslie, Aspects on reverberation modelling and inversion with physical scattering kernels, Proc. 16th ICSV. Krakow (2009).
15. H.L. Royden. Real Analysis, 2nd ed Macmillan. (1968)
16. F. Andersson, M. Carlsson and M.V. de Hoop, 'Nonlinear approximation of functions in two dimensions by sums of exponential functions', Appl.Comput.Harmon.Anal. 29 156-181. (2010)